Evaluation of subseasonal impacts of the MJO/BSISO in the East Asian extended summer

By

Chueh-Hsin Chang[1,2], Nathaniel C. Johnson[3], Changhyun Yoo[1,4]

[1]Center for Climate Change Prediction Research, Ewha Womans University, Seoul, Korea
[2]Department of Atmospheric Sciences, National Taiwan University, Taipei, Taiwan
[3]Princeton University/Geophysical Fluid Dynamics Laboratory, New Jersey, U.S.
[4]Department of Climate and Energy Systems Engineering, Ewha Womans University, Seoul, Korea

Corresponding author: Chueh-Hsin Chang (midicarcas@gmail.com)
Corresponding author: Changhyun Yoo (cyoo@ewha.ac.kr)

Abstract

The Madden-Julian Oscillation (MJO)/Boreal Summer Intraseasonal Oscillation (BSISO) has been considered an important climate mode of variability on subseasonal timescales for East Asian summer. However, it is unclear how well the MJO/BSISO indices would serve as guidance for subseasonal forecasts. Using a probabilistic forecast model determined through multiple linear regression (MLR) with MJO, ENSO, and long-term trend as predictors, we examine lagged impacts of each predictor on East Asia extended summer (May-October) climate from 1982 to 2015. The forecast skills of surface air temperature (T2m) contributed by each predictor is evaluated for lead times out to five weeks. We also provide a systematic evaluation of three commonly used, real-time MJO/BSISO indices in the context of lagged temperature impacts over East Asia.

It is found that the influence of the trend provides substantial summertime skill over broad regions of East Asia on subseasonal timescales. In contrast, the MJO influence shows regional as well as phase dependence outside the tropical band of the main action centers of the MJO convective anomalies. All three MJO/BSISO indices generate forecasts that yield high skill scores for week 1 forecasts. For some initial phases of the MJO/BSISO, skill reemerges over some regions for lead times of 3-5 weeks. This emergence indicates the existence of windows of opportunity for skillful subseasonal forecasts over East Asia in summer. We also explore the dynamics that contribute to the elevated skills at long lead times over Tibet and Taiwan-Philippine regions following the initial state of phases 7 and 5, respectively. The elevated skill is rooted in a wave train forced by the MJO convective heating over the Arabian Sea and feedbacks between MJO convection and SSTs in Taiwan-Philippine region. Two out of the three commonly used MJO/BSISO indices tend to identify MJO events that evolve consistently in time, allowing them to serve as reliable predictors for subseasonal forecasts for up to five weeks.

1. Introduction

The Madden-Julian Oscillation (MJO) is one of the dominant modes of climate variability on subseasonal timescales in the tropics. It is a planetary-scale convective anomaly consisting of an envelope of mesoscale convective systems coupled to large-scale circulation disturbance with coherent eastward propagating wind and precipitation signals along the equator with a period of 30-90 days. Over the broad tropical region, the MJO has two peak seasons with the strongest signals observed in boreal winter and second peak in boreal summer (Zhang and Dong 2004). In summer, the MJO exhibits additional northward propagation when interacting with the monsoon system in Asia (Lau and Chan 1986; Chen et al., 1988; Lawrence and Webster 2002; Fu and Wang 2004a). Because of this marked seasonality, in summer the MJO is also referred to the boreal summer intraseasonal oscillation (BSISO) (Straub and Kiladis 2003; Fu and Wang 2004a,b; Kikuchi et al. 2012; Li et al. 2017).

The MJO impacts various weather and climate patterns across the globe. For example, it modulates tropical cyclone (TC) activity in the Atlantic Ocean, the eastern North Pacific, the western North Pacific and the Indian Ocean (e.g., Klotzbath 2010, Maloney and Hartmann 2000, Li and Zhou 2013, Kikuchi and Wang 2010). Over India, Australia as well as subtropical east Asia, it is found that the summer monsoon onset timing is often associated with certain phases of the MJO (Bhatla et al. 2017; Taraphdar et al. 2018; Wheeler and McBride 2005; Chi et al. 2015). Furthermore, in Australia and Indian regions, active and break periods of summer monsoon rainfall are regulated by different phases of the MJO (Wheeler et al 2009; Evans et al. 2014; Pai et al. 2011). Convection anomalies associated with the MJO can influence weather and climate outside the tropics by forcing large-scale teleconnection patterns, such as the Pacific/North American pattern (PNA) (Mori and Watanabe 2008; Johnson and Feldstein 2010; Tseng et al. 2019). The thermal advection by the MJO-induced circulation anomalies plays a key role in modulating the surface temperature in the extratropics, including East Asia (Jeong et al. 2005 ; Yoo et al. 2012a). In summer, impacts of the MJO can also reach East Asia due to its northward propagation (e.g., Yasunari 1979; Wang et al. 2006; Chen et al. 2015).

Because of its periodicity and relationships with a wide range of weather and climate phenomena, the MJO has been considered as a major source of predictability on subseasonal timescales. There have been substantial advances in theoretical understanding and numerical simulation of this mode of variability. Considerable efforts have been made to understand the multivariate structure of the MJO and its propagation in observations and in dynamical models. Both climate research and forecasting communities hope that these developments may help to bridge the “predictability gap’’ between short-range deterministic weather forecasts and longer range probabilistic monthly and seasonal climate forecasts (Johnson et al. 2014). The challenge at these subseasonal timescales lies in overcoming the large error growth associated with the initial conditions and the short averaging time for slowly evolving climate signals to stand out clearly from the weather noise.

In order to characterize the MJO structure and to monitor its evolution in real-time, several MJO indices have been defined and applied in operational settings to increase subseasonal forecast potential. These indices include Wheeler and Hendon (2004) MJO index (WH MJO index hereafter), Kikuchi et al. (2012) bimodal tropical intraseasonal oscillation (ISO) index (Bimodal index hereafter), and Lee et al (2013) BSISO index (JYL BSISO index hereafter), Lin (2013) ISO index for the east Asia and western north Pacific (EAWNP) region (EAWNP ISO index hereafter) and Suhas et al (2013) Indian monsoon ISO index (Indian MISO index, hereafter). The WH MJO index is defined by the first two principal component time series of the multivariate empirical orthogonal function (MV-EOF) modes of the equatorial mean (between 15^{o}S and 15^{o}N) anomalous outgoing longwave radiation (OLR), and zonal winds at 850 hPa (U850) and 200 hPa (U200) (Wheeler and Hendon 2004). The Bimodal index is constructed by projecting unfiltered OLR anomalies onto the dominant tropical (between 30^{o}S and 30^{o}N) ISO spatial patterns obtained by applying the extended EOF (EEOF) approach to 25-90-day bandpass filtered OLR data (Kikuchi et al. 2012). Targeting Asia summer monsoon ISO, the JYL BSISO index is defined by the first two MV-EOF modes of anomalous OLR and U850 over Asia summer monsoon region (40^{o}E-160^{o}E, 10^{o}S-40^{o}N). The EAWNP ISO index is based on the first two MV-EOF modes of zonally averaged OLR and U850 anomalies in the EAWNP domain (90^{o}E-150^{o}E 10^{o}S-40^{o}N), whereas the Indian MISO index is constructed applying EEOF on zonally averaged rainfall anomaly over the Indian summer monsoon domain (60.5^{o}E-95.5^{o}E, 12.5^{o}S-30.5^{o}N). Note that the annual cycle as well as interannual and lower-frequency variabilities are removed from all five indices during the construction.

Although these indices intend to capture the same basic phenomenon, none of the indices perfectly captures the MJO owing to the limitations of the statistical methods that define them. No index captures the event-to-event differences in spatial structure, and all indices capture non-MJO variability to some extent. However, the life cycle composites of the convective anomalies based on each of these indices unveil some robust features of MJO propagation in boreal summer (e.g., Fig. 8b in Kikuchi et al (2012), Fig. 9 in Lee et al (2012), Fig.10 in Lin (2013), and Fig. 10 Suhas et al (2013)). In phase 1, enhanced convection appears in the equatorial central Indian Ocean. During phases 2-4, the convection anomaly propagates northward into the Indian subcontinent as well as eastward into the Bay of Bengal and the Maritime Continent. A northwest-southeast tilted rainband from the northern Indian Ocean to equatorial Pacific begins to emerge in phase 4. The eastern portion of the rainband intensifies as it reaches the South China Sea and the Philippine Sea in phases 5-6. The northward propagation also becomes prominent in the western Pacific (phases 6-8).

Such a propagating nature makes the MJO impact on regional weather and climate predictability sensitive to its phases (e.g., Lin et al., 2010; Johnson et al., 2014). The patterns of tropical convection associated with individual phases may preferentially influence particular regions remotely through teleconnection patterns or locally owing to its passage. In addition, given the slow propagation of the MJO and the timescale of several days for the atmosphere to respond to the convective heating (Hoskins and Karoly 1981), the local impacts associated with MJO phases may persist for several weeks (Johnson et al. 2014; Riddle et al. 2013; Tseng et al. 2018).

The discussion above suggests that indices monitoring the MJO in real-time may be useful for subseasonal forecast guidance. In the U.S., the National Oceanic and Atmospheric Administration (NOAA) Climate Prediction Center (CPC) has developed statistical forecast guidance derived from Johnson et al. (2014) to inform their Week 3-4 Outlooks, demonstrating the potential for statistical relationships rooted in the MJO, El Niño-Southern Oscillation (ENSO), and linear trend to enhance forecasts beyond two weeks. For East Asian winter, a similar statistical approach is applied using atmospheric teleconnection patterns as predictors (Yoo et al. 2018).

The present study addresses whether similar potential exists for East Asia summer. We develop a probabilistic forecast model determined through multiple linear regression (MLR) with the MJO, ENSO and linear trend as predictors for subseasonal temperature prediction. Because there exist multiple MJO/BSISO indices for summer, we also perform a systematic evaluation of the three most widely used MJO/BSISO indices of our interest as predictors: the Bimodal (Kikuchi et al. 2012), WH (Wheeler and Hendon 2004), and JYL (Lee et al. 2013) indices. We do not intend to inspect the fidelity of each of these MJO/BSISO indices in extracting the MJO signals nor do we attempt to investigate the strength and weakness of the individual index construction approach. Instead, we examine the lagged impacts of these three MJO/BSISO indices on East Asia extended summer (May – October) climate from 1982 to 2015. The forecast skills of surface air temperature (T2m) are evaluated for each phase of the indices for lead times out to five weeks. Throughout the article, we refer this dominant tropical 30-90 day ISO as MJO, unless the ISO indices are discussed, in which case, we refer to the index as MJO/BSISO.

We introduce the datasets and methods used in this study in section 2. We compare the forecast skill scores with different predictors as well as explore the dynamics that contribute to the elevated skills over various geographical regions in section 3. In section 4, we summarize our findings and discuss their implications.

2. Data and Methodology

2.1 Data

For the MLR prediction model, we use observed, daily MJO/BSISO and ENSO indices for May – October and 1982-2015 as predictors. As discussed in the introduction, we obtain three different MJO/BSISO indices: the Bimodal index (available at http://iprc.soest.hawaii.edu/users/kazuyosh/Bimodal_ISO.html), the JYL BSISO index (available at http://www.apcc21.org/eng/service/bsiso/moni/japcc030602.jsp), and the WH MJO index (available at http://www.bom.gov.au/climate/mjo/). For ENSO, we use daily SST anomalies averaged in the Niño 3.4 region (5°S - 5°N, 120° - 170°W) (Niño 3.4 index hereafter) derived from NOAA Optimum Interpolation Sea Surface Temperature Version 2 (OISSTv2; Banzon et al. 2016) and obtained at a 0.25° spatial resolution. For the Niño 3.4 index and all gridded data described subsequently, we determine anomalies by subtracting the first four harmonics of the 1982-2011 calendar day means.

We use the following gridded datasets in this study, with their horizontal resolutions noted in parentheses. For the atmospheric circulation fields, we use stream function at 850 hPa (ψ_{850}) and 300 hPa (ψ_{300}) (1.5°x1.5°) derived from the Interim European Centre for Medium-Range Weather Forecasts (ECMWF) Re-Analysis (ERA-Interim; Dee et al. 2011). For tropical deep convection, we use daily OLR (2.5°x2.5°) from NOAA (Liebmann and Smith 1996) as well as pentad precipitation data (2.5°x2.5°) from the Global Precipitation Climatology Project (GPCP) version 2.2 (Adler et al. 2003; Huffman et al. 2009). The ERA-Interim daily 2-m air temperature (T2m) (1°x1°) serves as the predictand in the MLR forecast models. For all analyses, we focus on a domain covering most of Southeast and East Asia, defined as 20°S-50°N, 60°-180°E.

To examine forecast sensitivity to different T2m datasets, we use two additional datasets: the fifth generation of ECMWF reanalysis data (ERA5; Hersbach et al. 2020) and the NASA's Modern-Era Retrospective Analysis for Research and Applications, version 2 (MERRA2; Gelaro et al., 2017). Both datasets are interpolated into the same horizontal and temporal resolutions as ERA-Interim T2m (1°x1°, daily).

2.2 Method

We generate weekly probabilistic T2m anomaly forecasts at each grid point through the following multiple linear regression (MLR) model for the time period of May-October 1982-2015:

$$T_{0+m} = \sum_i a_{i,m} P_{i,0} + b + \varepsilon \qquad (1)$$

In (1), T_{0+m} represents the mean of the predicted T2m distribution at lead m, a_i represents the regression coefficient for predictor, P_i, the subscript 0 indicates that the predictors are based on values at the initial time, b is the intercept term, and $\varepsilon \sim N(0, \sigma_{0+m})$ (see (2)) is a Gaussian residual. In this study, the predictors include the MJO/BSISO index, the Niño 3.4 index, and time, t. For each grid point we assume a Gaussian distribution of the predicted T2m anomaly with the standard deviation that accounts for both error in the model and the future observation:

$$\sigma_{o+m} = \sqrt{\hat{\sigma}^2 x_0'(X'X)^{-1} x_0} \quad (2)$$

where σ_{0+m} is the predicted standard deviation, $\hat{\sigma}^2$ is the mean square error, X is the predictor matrix, and x_0 is the predictor values in column vector form. The predictor matrix X is a T x 5 matrix, where T is the total number of daily observations in the training data and the 5 columns consist of a column of ones, the two MJO/BSISO index components, the Niño 3.4 index, and time. The predictor vector x_0 consists of 1 and the four predictor values for the forecast.

For verification purpose, a leave-one-year-out cross-validation approach is applied: the year *n* forecasts are made based on the statistics of data from all other years and then verified using the data of year *n*. The weekly forecasts are initialized on each day from 1 May through 31 October for the years 1982-2015. The forecasts are conducted for lead times of one to five weeks. For example, for forecasts initialized on 1 May 1982, week one forecast covers the first week (2-8 May 1982) following the initialization day, week two forecast covers the second week (9-15 May 1982) following the initialization, and so on.

We divide the forecasts into three categories with equal probabilities over the 1982-2011 base period. The three categories are: below normal, near normal and above normal, where "normal" is defined as the calendar week climatology of the base period. For the tercile boundaries, we first pool together five days of T2m anomalies centered on the forecast date from 1982 to 2011 and calculate the 33.33rd and 66.67th percentiles of these T2m anomalies. "Below", "near" and "above" normal temperatures are defined by the bottom, middle and top terciles of the climatological (base period) T2m distribution, respectively.

We evaluate our forecasts using Heidke skill score (HSS), which measures the fraction of correct forecasts after excluding those being correct by chance. For this measure, each probabilistic forecast is assigned to one of the three forecast categories based on the highest of the three forecast probabilities. The HSS formula is then expressed as

$$HSS = \frac{(H-E)}{(A-E)} \times 100 \quad (3)$$

where *H* represents the number of correct forecasts and *E* is the expected number of correct forecasts by chance (one-third of the total number of forecasts, *A*). The HSS ranges in value from –50 (all incorrect forecasts) to 100 (all correct forecasts), and HSS values greater than zero indicate skill relative to a random forecast.

We also use the ranked probability skill score (RPSS) as a second measure of forecast skill. The RPSS explicitly accounts for the difference between the verified category and probabilities for each of the three categories. Specifically, RPSS is based on the sum of squared differences between the components of the cumulative forecasts and observations (the ranked probability score, or RPS). If we express the forecast as a three-element vector *F* with the ordered probabilities for each category, and similarly the verified observations as a vector *V* with a component value of 1 for the verified forecast category and 0 otherwise, then the RPS is expressed as

$$RPS = \sum_{i=1}^{3}\left(\sum_{j=1}^{i} F_j - \sum_{j=1}^{i} V_j\right)^2 \tag{4}$$

The RPSS is then calculated as

$$RPSS = 1 - \frac{\langle RPS \rangle}{\langle RPS_{clim} \rangle} \tag{5}$$

where angle brackets define a time average, and RPS_{clim} is the RPS for a climatological forecast (33.3% for each category). Therefore, RPSS values greater than 0 indicate skill relative to a climatological forecast. These are two of the most commonly used metrics in operational forecast centers. For example, in the NOAA CPC Verifications page (https://www.cpc.ncep.noaa.gov/products/verification/summary/), HSS and RPSS are the two metrics that are provided.

We evaluate the statistical significance of the HSS frequencies through a Monte Carlo simulation approach. For each simulation, we randomly reshuffle both forecast and verified years and then generate resampled forecast and verification data with the reshuffled years. We then calculate the HSS of the resampled forecast/verification data pair in the same way as with the true forecasts and verification. We repeat these simulations 1000 times and calculate the 95th percentiles of the synthetic scores. The HSS is considered statistically significant at the 5% level (one-tailed test) if it exceeds the 95th percentile of the synthetic scores at that grid point. These calculations are made only for the first forecast lead, given the computational expense and the expectation that the threshold for significance should not depend on lead time.

3. Results

The full forecasts determined through our MLR model incorporate information of the MJO, ENSO, and long-term trend. To evaluate the overall forecast performance contributed by these potential sources, we first examine the mean HSS map for all the forecast days for the extended summer (May-October) during 1982-2015 over the East Asia Domain. Figure 1 is obtained by averaging the skill across three sets of forecasts with different MJO/BSISO indices. Each of the MJO/BSISO indices yields similar general patterns of skill but with some notable differences that we discuss more thoroughly below. The variability in skill among the three indices is much smaller than the average skill (not shown), indicating that the results are robust to the choice of index (Figs 1a,c,e). Substantial skills (HSS > 15) persist through at least week 5 over the tropical band (±10°), northwestern Indochina peninsula, including Bangladesh, Bhutan, northeastern India and Myanmar (15°N-30°N, 90°E-100°E), and the region extending southeast from the Maritime Continent, including the Solomon Islands and Fiji. Figures 1b,d,f show the mean RPSS. Comparison between the left and right halves of Figure 1 reveals that both metrics produce consistent patterns, indicating that interpretations are not sensitive to evaluation method. The persistence of elevated skill through week 5 in some regions indicates the importance of low-frequency sources of skill, such as ENSO or long-term trend, but the higher-frequency MJO also is an important source of skill within parts of East Asian domain, as discussed in Section 3.2.

3.1 Forecast Evaluation

In the following, we examine the forecast skills contributed by each predictor. These contributions are determined by calculating the skill in the MLR model that excludes the target predictor from that of the full MLR model. In Figure 2 we explore ENSO and the linear trend influences. Because both ENSO and the linear trend evolve slowly, their related skills do not change much with increasing lead times on subseasonal timescales (not shown). We therefore focus only on one lead, week one. Figure 2a shows the map of HSS difference (ΔHSS) between forecasts with and without the ENSO predictor. The influence of ENSO is weak except in the tropical region, especially south of the equator. The tropical band of relatively high skill (HSS > 3) is colocated with the substantially negative T2m regressions on the Niño 3.4 index (< –0.1°C) (Fig. 2c). This result suggests that ENSO has a weak influence on East Asian temperature in the boreal summer, which is consistent with earlier studies on ENSO impacts (e.g. Halpert and Ropelewski 1992).

The linear trend of T2m shows warming signal throughout much of the East Asian domain (Fig. 2d). The uniformity of sign and the enhanced warming of land relative to ocean is consistent with the impact of increasing greenhouse gases. The existence of substantial spatial heterogeneity relative to the more uniform radiative forcing likely owes to the influence of internal climate variability in the short observational record or to uncertainties in the data record. To explore the latter source, we show in Figure 3 the ΔHSS maps of the full T2m forecasts using ERA5 (Fig. 3a) and MERRA (Fig 3b) relative to that of ERA-Interim for week one. The regions of insignificant HSS in the ERA-Interim-derived forecasts are masked out. Regions of large difference ($|\Delta HSS|$ > 10) are seen over the tropical band east of 150°E, northwestern Indochina peninsula, southern Indian Ocean and mid-latitude East Asia, indicating sensitivity to T2m dataset. The differences between MERRA- and ERA-Interim-derived forecasts are particularly pronounced (Fig 3b). This analysis reveals sensitivity to the choice of T2m dataset, but the results are robust for the regions and patterns discussed in the remainder of this study.

The high skill (HSS > 10) regions revealed in the ΔHSS map between forecasts with and without the linear trend predictor include those identified by the full forecast result in Figure 1: the tropical band, northwestern Indochina peninsula and southeast extension from the Maritime Continent. We also see an additional high skill region contributed by the trend predictor over the mid-latitude East Asia (90°E-120°E) (see Fig. 2d). Most notable for the purpose of this study, the influence of the trend (that is linearly independent of all other predictors) provides substantial summertime skill over broad regions of East Asia. The strong skill even on subseasonal timescales in some regions likely is the result of the trend signal standing out more cleanly above the noise of random weather variability in the summertime than in other seasons, when midlatitude dynamics are more vigorous. These findings do not change if we extend the period of analysis to 2018, which would add the extreme El Niño of 2015-16 and subsequent post-global warming “hiatus” period (not shown).

3.2 MJO/BSISO Index Comparison

We now examine the impacts of MJO on subseasonal forecast skill and the difference caused by the choice of MJO/BSISO indices. Figure 4 shows the ΔHSS map between forecasts with and without MJO/BSISO indices for all three indices for both short (week 1) and long (skill averaged over weeks 3-4) lead times. A dominant zonal band of enhanced skill (HSS > 6) is seen along the equator from the Indian subcontinent to the Maritime Continent, with even higher skill (HSS > 9) over the tropical oceanic regions (Figs. 4a,c,e). It is robust for both short (week 1) and long (weeks 3-4) lead times (Figs. 4b,d) except for JYL BSISO index for weeks 3-4 (Fig. 4f). Upon close inspection, another zonal band of enhanced skill (HSS > 3) can be seen outside the tropics from Tibetan Plateau stretching southeastward to Taiwan-Philippine region for week 1 (Figs. 4a,c,e). The skill of this band reemerges at the long lead time for the Bimodal and WH MJO indices (Figs. 4b,d). The distinct geographical locations of the two zonal bands suggest two pathways for the enhanced skills contributed by the MJO. The tropical band is colocated with the main action centers of the MJO convective anomalies, and so it likely represents a direct response to the MJO tropical dynamics. The fact that the highest skill is over the oceanic regions in the tropical band reflects that the tropical response is strongly contributed by SST anomalies produced during MJO events, as discussed in previous studies (e.g. Maloney and Kiehl 2002; Gao et al 2019). The extratropical band, on the other hand, is separate from the MJO action centers, and likely represents a more indirect teleconnection in response to the circulation anomalies excited by the MJO convection.

After comparing individual indices, we also consider the performance of the ensemble mean forecasts relative to that of each individual model. We calculate the ensemble mean by averaging the probabilities among the three models that differ only in choice of MJO index. Figure 5 shows the ΔHSS map between the ensemble mean performance and that of individual models, including bimodal (top), WH (middle) and JYL (bottom), respectively. It is seen that the ensemble forecast only performs noticeably better than the JYL model (Fig 5c) but not better than the WH (Fig 5b) or bimodal models (Fig 5a). Hence there is no clear advantage to using a multimodel ensemble for this particular statistical forecast model.

For the purpose of our study, the extratropical band is of particular interest because not only it is located in East Asia but also the elevated forecast skill brought about by the MJO is seen for both short and long lead times, although the skill decays more quickly for the JYL index than for the other two. In addition, these two regions are also among those least sensitive to the choice of datasets ($|\Delta HSS| < 5$, Fig 3). In the following we explore the regional MJO-related skill variations with respect to fo recast lead times and the associated dynamics with the focus on the two areas in the extratropical band: (1) Tibetan Plateau (90°E-100°E, 26°N-32°N), and (2) Taiwan-Philippine region (117°E-132°E, 16°N-25°N) (marked by the green boxes in Figure 4).

The line plots in Figure 6 show the mean HSS averaged over Tibetan and Taiwan-Philippine boxes for forecasts using three different MJO/BSISO indices with respect to lead times (color lines). For comparison, the regional box-averaged mean HSS for forecasts without MJO/BSISO is also included (dashed line). The HSS curve of no-MJO/BSISO exhibits the lowest values throughout the forecast time period: HSS < 7 (Fig. 6a) and HSS $\leq$ 0 (Fig. 6b) in Tibet and Taiwan-Philippine regions, respectively. The dominant contribution of the MJO/BSISO to the forecast skills in these regions is apparent from the distance between the color and dashed lines.

In general, the skill score that includes MJO as predictor decreases as lead time increases (Fig. 6). However, close inspection of the three HSS curves of different MJO/BSISO predictors reveals notable differences. The skill score of JYL BSISO curve drops more rapidly than the other two curves in both regions (red curve in Figs. 6a-b). Another two notable differences in Figure 6 are the gentle decrease of Bimodal index in the Tibet region from week 2 to week 4 (blue curve in Fig. 6a) and WH MJO skill reemergence at week 2 in Taiwan-Philippine region (green curve in Fig. 6b). These results suggest that potentially useful skill persists for several weeks at these two locations, but the level of skill provided by the statistical forecast guidance may be sensitive to the choice of MJO/BSISO index.

3.3 Contributing Mechanisms

Next, we investigate individual MJO phases that contribute to the elevated skills at longer lead times and the associated dynamics in Tibet and Taiwan-Philippine regions. We inspect the regional box-averaged HSS variation with lead time for each phase of the MJO/BSISO. Inspection of the HSS curves for each MJO/BSISO phase (not shown) reveals phase-dependent skill enhancement beyond week 2, suggesting windows of opportunity for skillful weeks 3-5 forecasts for certain initial MJO/BSISO phases. For the Tibet region, these windows of opportunity correspond with initial phases 7 and 8, as we see HSS values exceeding 15 with the Bimodal index predictor at lead times of 3-4 weeks (blue curves in Figs. 7a-b). In Taiwan-Philippine region, these windows of opportunity are associated with phases 5 and 6 at lead times of 2-4 weeks based on Bimodal and WH MJO indices, respectively (blue and green curves in Figs. 9a-b).

To understand the mechanisms responsible for such skill reemergence, we examine the event evolution after the initial state of these phases through lagged composite analysis. We calculate composites following the Bimodal index phase 7 (5) for Tibet (Taiwan-Philippine) region by averaging 370 (391) days when the amplitude of the MJO/BSISO phase is greater than 1. Figures 7c-h and 8a-c show the 7-day composite anomalies of T2m, OLR and 300 hPa stream function (ψ_{300}) for initial state of phase 7 and for lags of zero to five weeks based on the Bimodal index. It is seen that three weeks after the initial state of phase 7 at lag 0 (Fig. 7c) the composite MJO anomalies flip sign with cold T2m and negative OLR anomalies dominating tropical Indian Ocean and south Bay of Bengal (Fig. 7f). An area of enhanced cold T2m anomaly (< -0.4^{o}C) appears over the Tibet region in week 4 (Fig 7g) and lasts for two weeks (Fig 7h). In the dynamical field, as the convective anomaly moves to the Arabian Sea at lag 4, it forces an upper-level wave train pattern to the northeast and extending to Japan (Fig 8b). We see that a pair of circulation anomalies embedded in the wave train, with anticyclonic anomaly over the Indian subcontinent and cyclonic anomaly over the central-eastern parts of China, advects cold air from the north to the Tibet region (Fig. 7g, Fig. 8b). The cold T2m anomaly intensifies and persists for two weeks (Fig. 7h), reflecting in the elevated skill at weeks 4 and 5 in Figure 7a (blue curve). The lagged composite maps for phase 8 are similar to those of phase 7 (not shown).

We repeat the same composite analysis for the Bimodal index phase 5 to target the sources of elevated skill in the Taiwan-Philippine region (Fig. 9). As seen at the initial time and persisting through the second week, a northwest-southeast tilted band of negative OLR and T2m stretches from the Indian subcontinent through the Bay of Bengal and southern part of the South China Sea to the western tropical Pacific (Figs. 9c-d). The convective band, though much weaker, reaches Taiwan-Philippine region by week 3 (Fig. 9f). The enhanced convection (negative OLR anomalies in Fig. 9f and positive precipitation anomalies in Fig. 10c) over this maritime region may contribute to T2m cooling through its influence on SST, including reduced shortwave radiation into the ocean due to cloudiness and enhanced latent heat flux out of the ocean through wind anomalies (DeMott et al. 2015; Gao et al. 2019). It can also contribute to cold T2m anomalies through cold advection associated with cyclonic circulation anomaly, indicated by the negative ψ_{850} centered northeast of the region (Fig. 10c). Ultimately, the MJO-induced convective anomaly leads to a prolonged imprint on the regional T2m anomaly pattern at weeks 3 and 4, as seen in yellow box region in Figures 9f-g, even after the convective band dissipates by week 4 (Figs. 9g, 10d). The window of forecast opportunity brought about by this sequence of events is clearly seen at weeks 3-4 in Figure 9a (blue curve). The lagged composite maps for WH MJO phase 6 produce a similar sequence and yield the same interpretation (not shown).

4. Discussion and Conclusion

The MJO has been considered an important climate mode of variability on subseasonal timescales for East Asian summer. Several indices have been constructed to monitor the MJO in real time, but it is unclear how well they serve as guidance for subseasonal forecasts. Our study systematically evaluates the lagged surface air temperature impacts of the three MJO/BSISO indices commonly used in operational settings. We identify the regions and MJO initial states where inclusion of MJO information provides windows of opportunity for skillful forecasts at lead times extending beyond the timescale of traditional weather forecasts. We then examine lagged composites corresponding with these MJO initial phases over selected regions of interest to decipher the sources of elevated skill at these subseasonal lead times.

Overall, our study indicates the potential to develop skillful subseasonal forecast guidance over some regions of East Asia in boreal summer with the use of a linear statistical model. Most previous studies have focused on the boreal winter (e.g., Johnson et al. 2014; Yoo et al. 2018), when Northern Hemisphere tropical-extratropical midlatitude interactions are strongest and the potential for extended-range skill rooted in the tropics appears to be highest. However, in boreal summer, the influence of the MJO combined with the long-term warming trend is also strong and persistent enough to provide a reliable source of subseasonal forecast skill, at least in some regions and for some initial phases of the MJO.

Our study offers an objective approach to tease out relevant predictors and the resulting windows of opportunity at subseasonal lead times. For instance, in our study, we examine forecast skills associated with each phase of the observed MJO and find that the contribution from individual phases varies. Such an approach can be applied to forecast model data as well to examine model biases and performance. For example, a model may score high at certain phases of MJO but low at others. The difference may help identify the essential physical processes that are not simulated or understood previously.

We also provide a systematic evaluation of three commonly used, real-time MJO/BSISO indices from the perspective of lagged temperature impacts over East Asia. Although the three indices intend to extract similar MJO signals, the differences in how they are defined result in distinct lagged temperature impacts over East Asia, as indicated by differences in forecast skills when used as predictors in the statistical forecast model. For the purpose of subseasonal prediction, it is desirable to choose an index that captures longer-lasting organized signals in order to achieve higher skills for longer lead times. As seen in Figure 4, the pattern of skills provided by JYL BSISO predictor disintegrates by weeks 3-4 (Fig. 4f), whereas those associated with the Bimodal and WH MJO predictors remain organized (Figs. 4d-e). Furthermore, the mean HSS of JYL BSISO index over the regions of our interest declines more rapidly than other two indices (Fig. 6).

A recent study alluded to the limited applicability of the JYL index for subseasonal forecast guidance. They find that the JYL index shows standing wave characteristics with little propagation (Wang et al. 2018). To further understand the nature of this distinction, we explore the ability of each index to track strong MJO events with a well-defined timescale. Though varying from event to event, the transition between each phase on average is about 5-7 days during an MJO (Wheeler and Hendon 2004; Kikuchi et al 2012). With data of weekly temporal resolution, one would expect the fields to resemble phase 2 one week after the onset of phase 1. Likewise, phase 3 would emerge two weeks after phase 1 onset, and so on. We calculate the pattern correlation (γ) between OLR composite of each phase and the corresponding lagged composites with respect to phase 1 for all three MJO indices to examine how well a specific index tracks consistently evolving MJO events. Figure 11 shows such a comparison between phase 3 and lag 2 composite of phase 1 for bimodal (top), WH (middle), and JYL (bottom) indices. The similarities between phase 3 (left column) and its respective lagged composite of phase 1 (right column) are indicated by the pattern correlation coefficients: 0.94, 0.80, and 0.55 for bimodal, WH, and JYL indices, respectively. Figure 12 summarizes the decrease in pattern correlation for each index with respect to time/phase; that is, declining in the ability of each index to track the MJO as it propagates. It is seen that the bimodal and WH indices are able to track relatively closely the MJO for five weeks ($\gamma \geq 0.7$), whereas γ for JYL index drops sharply after one week (≤ 0.55). These findings indicate that the bimodal and WH indices tend to identify events that evolve rather consistently in time, allowing them to serve as reliable predictors for subseasonal forecasts for up to five weeks.

Such a distinction may be caused by the different domain selection for the index construction. As pointed out in the introduction, JYL BSISO index targets the Asia summer monsoon ISO and the domain is confined to the Asia longitudes (40ºE—160ºE), instead of the circumglobal domain like Bimodal and WH MJO indices. It is also worth mentioning that besides filtering out the interannual and other lower frequency signals, in the Bimodal and WH MJO cases, additional spatial filtering procedures are applied prior to construction of real-time indices. The WH index is based on the equatorial mean (averaged between 15ºS and 15ºN) variables whereas the Bimodal index is constructed through projection onto the spatial MJO pattern of 25-90-day bandpass filtered data (see Introduction for details). By focusing on the large-scale coherent spatial structure of convection and circulation associated with the MJO, higher frequency variability is removed without employing conventional time filters (Kikuchi et al. 2012). This spatial filtering effect may also be a potential contributor to the marked difference between JYL BSISO index and the other two indices. Lastly, for the focus of our study, Bimodal index achieves overall higher scores in our evaluation for subseasonal T2m forecast in East Asia summer. It is likely because of the EEOF approach and exclusion of 10-20 day bi-weekly Rossby waves during its construction. The EEOF approach tends to pick out persistent MJO events, and the 10-20 day bi-weekly Rossby wave is another dominant subseasonal oscillation in East Asia (Kikuchi et al. 2012; Li and Zhou 2013).

The mechanisms by which the MJO contributes to subseasonal forecast skill remain an active area of investigation. Recent studies identify the sources of skill for extratropics associated with consistent teleconnection patterns forced by certain phases of the MJO over the Indian Ocean and western Pacific (Seo and Lee 2017; Tseng et al. 2019). On the other hand, phase-dependent MJO-driven inertio-gravity waves are found to degrade forecast skill in the extratropics (Rodwell et al. 2013; Franzke et al. 2019). Forecast errors in the MJO extratropical response may arise due to failure to consider the evolution of the MJO (Yadav and Straus 2017; Goss and Feldstein 2018) and the extratropical base states (Goss & Feldstein, 2015; Henderson et al., 2017). Our statistical forecast model only accounts for the initial state of the MJO/BSISO and not the detailed information of an MJO/BSISO, such as propagation speed and evolution, which can vary from event to event. Accounting for prior MJO evolution may offer little benefit because some evidence suggests that the extratropical response is insensitive to the MJO propagation speed (Goss and Feldstein 2018), and so the initial MJO state may provide sufficient information on the MJO convective forcing. Nevertheless, accurate information on the future evolution of the MJO likely would be beneficial (Zhang and Chang 2019), given that state-of-the-art dynamical forecast models can skillfully predict the summertime MJO out to 2-3 weeks (Lee et al. 2015; Fang et al. 2019). There are, however, additional sources of uncertainty such as synoptic-scale eddies that may degrade our model performance.

Given the relatively modest MJO-induced temperature impacts in tropical oceanic regions (O(0.1°C), Fig. 9), extensions of this model to other variables that show stronger signals associated with the MJO such as precipitation may yield even greater benefits. Finally, while there are windows of opportunity for enhanced subseasonal forecast skill when certain phases of MJO are active, MJO is inactive a large fraction of the time. There might be other sources of skill during the inactive phases of MJO. Future work may explore other mechanisms and indices to improve subseasonal statistical forecasts that may serve as operational guidance.

Acknowledgement

We thank Drs. June-Yi Lee, Matthew C. Wheeler and Kazuyoshi Kikuchi for insightful discussion about MJO monitoring and Drs. Chung-Hsiung Sui, Meng-Ming Lu, Pang-Chi Hsu, Yu Kosaka, and Ziqian Wang for constructive comments. We also thank three anonymous reviewers for helpful comments that improved this manuscript. This study was supported by National Research Foundation of Korea through grant NRF-2018R1A6A1A08025520 and NRF-2019R1C1C1003161. C-H Chang is also supported by MOST 106-2111-M-002-003-MY2 from the Ministry of Science and Technology of Taiwan. N. C. Johnson was supported by awards NA14OAR4320106 and NA18OAR4320123 from the NOAA, U.S. Department of Commerce.

References

Adler RF et al. (2003) The version-2 global precipitation climatology project (GPCP) monthly precipitation analysis (1979-present). J Hydromet 4:1147–1167

Banzon V, Smith TM, Chin TM, Liu C, Hankins W (2016) A long-term record of blended satellite and in situ sea-surface temperature for climate monitoring, modeling and environmental studies. Earth Syst Sci Data 8(1):165–176

Bhatla R, Singh, M, Pattanaik, DR (2017) Impact of Madden-Julian oscillation on onset of summer monsoon over India. Theor Appl Climatol 128: 381-391

Chen, T-C, Tzeng, R-Y, Yen, M-C (1988) Development and life cycle of the Indian Monsoon: Effect of the 30–50 day oscillation. Mon Wea Rev 116: 2183–2199

Chen J, Wen Z, Wu R, Chen Z, Zhao P (2015) Influences of northward propagating 25–90-day and quasi-biweekly oscillations on eastern China summer rainfall. Clim Dyn 45:105–124

Chi Y, Zhang F, Li W, He J, Guan Z (2015) Correlation between the onset of the East Asian subtropical summer monsoon and the eastward propagation of the Madden-Julian oscillation. J Atmos Sci 72:1200–1214

Dee D et al (2011) The ERA-Interim reanalysis: configuration and performance of the data assimilation system. Quart J Roy Met Soc 137:535–597

DeMott CA, Klingaman NP, Woolnough SJ (2015) Atmosphere-ocean coupled processes in the Madden-Julian oscillation. Rev Geophys 53:1099–1154

Evans S, Marchand R, Ackerman T (2014) Variability of the Australian monsoon and precipitation trends at Darwin. J Climate 27:8487–8500

Fang Y, Li B, Liu X (2019) Predictability and Prediction Skill of the Boreal Summer Intra-Seasonal Oscillation in BCC_CSM Model. J Meteorol Soc Japan 97:295-311

Franzke CLE, Jelic D, Lee S, Feldstein SB (2019) Systematic decomposition of the MJO and its Northern Hemispheric extratropical response into Rossby and inertio-gravity components. Q J R Meteorol Soc 145: 1147–1164

Fu X, Wang B (2004a) Differences of boreal summer intraseasonal oscillations simulated in an atmosphere–ocean coupled model and an atmosphere-only model. J Clim 17:1263–1271

Fu X, Wang B (2004b) The boreal-summer intraseasonal oscillations simulated in a hybrid coupled atmosphere-ocean model. Mon Wea Rev 132:2628-2649

Gao Y, Klingaman NP, DeMott CA, Hsu PC (2019) Diagnosing ocean feedbacks to the BSISO: SST-modulated surface fluxes and the moist static energy budget. J Geophys Res Atmos 124:146–170

Goss M, and Feldstein SB (2015) The impact of the initial flow on the extratropical response to Madden–Julian oscillation convective heating. Mon Wea Rev 143: 1104–1121

Goss M, and Feldstein SB (2018) Testing the sensitivity of the extratropical response to the location, amplitude, and propagation speed of tropical convection. J Atmos Sci 75: 639–655

Halpert MS, Ropelewski CF (1992) Surface temperature patterns associated with the southern oscillation. J Clim 5:577–593

Henderson SA, Maloney ED, Son S-W (2017) Madden–Julian oscillation Pacific teleconnections: the impact of the basic state and MJO representation in general circulation models. J Clim 30:4567–4587

Hoskins BJ, Karoly DJ (1981) The steady linear response of a spherical atmosphere to thermal and orographic forcing. J Atmos Sci 38(6):1179–1196

Huffman GJ et al. (2009) Improving the global precipitation record: GPCP version 2.1. Geophys Res Lett 36:L17808

Jeong J-H, Ho C-H, Kim B-M, Kwon W-T (2005) Influence of the Madden-Julian Oscillation on wintertime surface air temperature and cold surges in east Asia. J Geophys Res: Atmos 110:D11104. doi: 10.1029/2004JD005408

Johnson NC, Feldstein SB (2010) The continuum of North Pacific sea level pressure patterns: intraseasonal, interannual, and interdecadal variability. J Clim 23:851–867

Johnson NC, Collins DC, Feldstein SB, L'Heureux ML (2014) Skillful wintertime North American temperature forecasts out to 4 weeks based on the state of ENSO and the MJO. Wea Forecast 29:23–37.

Kikuchi K, Wang B (2010) Formation of tropical cyclones in the northern Indian Ocean associated with two types of tropical intraseasonal oscillation modes. J Meteor Soc Jpn 88:475–496

Kikuchi K, Wang B, Kajikawa Y (2012) Bimodal representation of the tropical Intraseasonal oscillation. Clim Dyn 38:1989–2000

Kikuchi K, Kodama C, Nasuno T, Nakano M, Miura H, Satoh M, Noda AT, Yamada Y (2017) Tropical intraseasonal oscillation simulated in an AMIP-type experiment by NICAM. Clim. Dyn. 48:2507–2528

Klotzbach PJ (2010) On the Madden–Julian oscillation–Atlantic hurricane relationship. J Clim 23:282–293

Lawrence DM, Webster PJ (2002) The boreal summer intraseasonal oscillation: relationship between northward and eastward movement of convection. J Atmos Sci 59:1593–1606

Lau WKM, Chan PH (1986) Aspects of the 40–50 day oscillation during the northern summer as inferred from outgoing long wave radiation. Mon Weather Rev 114:1354–1367

Lee JY, Wang B, Wheeler MC, Fu X, Waliser DE, Kang IS (2013) Real-time multivariate indices for the boreal summer intraseasonal oscillation over the Asian summer monsoon region. Clim Dyn 40(1):493–509

Lee S-S, Wang B, Waliser DE, Neena JM, Lee J-Y (2015) Predictability and prediction skill of the boreal summer intraseasonal oscillation in the Intraseasonal Variability Hindcast Experiment. Clim Dyn 45:2123–2135

Lee SS, Moon JY, Wang B, Kim HJ (2017) Subseasonal prediction of extreme precipitation over Asia: boreal summer intraseasonal oscillation perspective. J Clim 30:2849–2865

Liebmann B, Smith CA (1996) Description of a complete (interpolated) outgoing longwave radiation dataset. Bull Am Meteor Soc 77:1275–1277

Li RC, Zhou W (2013) Modulation of western North Pacific tropical cyclone activity by the ISO. Part I: genesis and intensity. J Clim 26:2904–2918

Li X, Gollan G, Greatbatch RJ, Lu R (2018) Intraseasonal variation of the East Asian summer monsoon associated with the Madden–Julian Oscillation. Atmos Sci Lett 19:e794. https ://doi.org/10.1002/asl.794

Li X, Gollan G, Greatbatch RJ, Lu R (2019) Impact of the MJO on the interannual variation of the Pacific–Japan mode of the East Asian summer monsoon. Clim Dyn 52:3489-3501

Lin H, Brunet G, Mo R (2010) Impact of the Madden–Julian Oscillation on wintertime precipitation in Canada. Mon Weather Rev 138(10):3822–3839

Lin H (2013) Monitoring and Predicting the Intraseasonal Variability of the East Asian–Western North Pacific Summer Monsoon. Mon Weather Rev 141:1124–1138

Maloney ED, Hartmann DL (2000) Modulation of hurricane activity in the Gulf of Mexico by the Madden-Julian oscillation. Science 287:2002–2004

Maloney ED, Kiehl JT (2002) MJO-Related SST Variations over the Tropical Eastern Pacific during Northern Hemisphere Summer. J Clim 15: 675–689

Mori M, Watanabe M (2008) The growth and triggering mechanisms of the PNA: a MJO–PNA coherence. J Meteor Soc Jpn 86:213–236

Pai DS, Bhate J, Sreejith OP, Hatwar HR (2011) Impact of MJO on the intraseasonal variation of summer monsoon rainfall over India. Clim Dyn 36(1):41–55

Riddle EE, Stoner MB, Johnson NC, Heureux MLL, Collins DC, Feldstein SB (2013) The impact of the MJO on clusters of wintertime circulation anomalies over the North American region. Clim Dyn 40:1749–1766

Rodwell MJ, Magnusson L, Bauer P, Bechtold P, Bonavita M, Cardinali C, Diamantakis M, Earnshaw P, Garcia-Mendez A, Isaksen L, Källén E, Klocke D, Lopez P, McNally T, Persson A, Prates F, Wedi N (2013) Characteristics of occasional poor medium-range weather forecasts for Europe. Bull Am Meteorol Soc 94(9):1393–1405

Seo K-H, Lee H-J (2017) Mechanisms for a PNA-Like Teleconnection Pattern in Response to the MJO. J Atmos Sci 74:1767–1781

Straub KH, Kiladis GN (2003) Interactions between the boreal summer intraseasonal oscillation and higher-frequency tropical wave activity. Mon Weather Rev 131:945–960

Suhas E, Neena JM, Goswami BN (2013) An Indian monsoon intraseasonal oscillations (MISO) index for real time monitoring and forecast verification. Clim Dyn 40: 2605–2616

Taraphdar S, Zhang F, Leung LR, Chen X, Pauluis OM (2018) MJO affects the monsoon onset timing over the Indian region. Geophysical Research Letters 45: 10,011–10,018

Tseng K-C, Barnes EA, Maloney ED (2018) Prediction of the midlatitude response to strong Madden-Julian oscillation events on S2S time scales. Geophys Res Lett 45: 463–470

Tseng K-C, Maloney ED, Barnes EA (2019) The consistency of MJO teleconnection patterns: an explanation using linear Rossby wave theory. J Clim 32: 531–548

Wang B, Webster P, Kikuchi K, Yasunari T, Qi Y (2006) Boreal summer quasi-monthly oscillation in the global tropics. Clim Dyn 7:661–675

Wang S, Ma D, Sobel AH, Tippett MK (2018) Propagation Characteristics of BSISO Indices. Geophys Res Lett. https://doi.org/10.1029/2018GL078321

Wheeler MC, Hendon HH (2004) An all-season real-time multivariate MJO index: development of an index for monitoring and prediction. Mon Weather Rev 132:1917–1932

Wheeler MC, McBride JL (2005) Australian-Indonesian monsoon. In: Intraseasonal Variability in the Atmosphere-Ocean Climate System. Springer Praxis Books (Environmental Sciences). Springer, Berlin, Heidelberg

Wheeler MC, Hendon HH, Cleland S, Meinke H, Donald A (2009) Impacts of the Madden–Julian oscillation on Australian rainfall and circulation. J Clim 22:1482–1498

Yadav P, Straus DM (2017) Circulation response to fast and slow MJO episodes. Mon Weather Rev 145(5):1577–1596

Yasunari T (1979) Cloudiness fluctuations associated with the northern hemisphere summer monsoon. J Meteorol Soc Jpn 57:227–242

Yoo C, Lee S, Feldstein S (2012) Mechanisms of Arctic surface air temperature change in response to the Madden–Julian Oscillation. J Clim 25:5777–5790

Yoo C, Johnson NC, Chang C-H, Feldstein SB, and Kim Y-H (2018) Subseasonal Prediction of Wintertime East Asian Temperature Based on Atmospheric Teleconnections. J Clim 31: 9351-9366

Zhang C, Dong M (2004) Seasonality in the Madden–Julian oscillation. J Clim 17:3169–3180

Zheng C, Chang EKM (2019) The role of MJO propagation, lifetime, and intensity on modulating the temporal evolution of the MJO extratropical response. J Geophys Res 124(10): 5352–5378

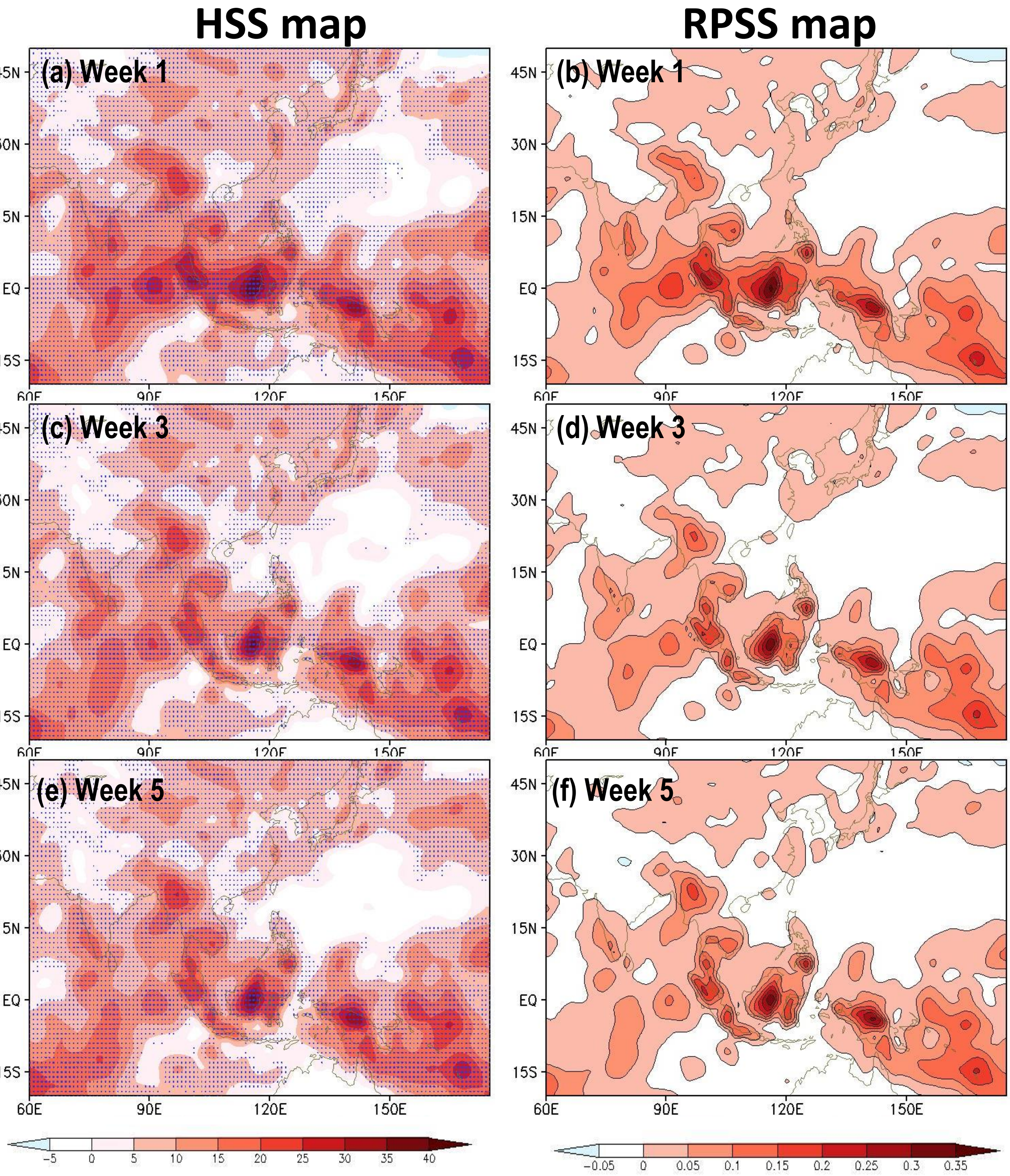

Figure 1. Average T2m forecast performance of the MLR forecast model. The May – October 1982-2015 mean (left) HSS and (right) RPSS for (a,b) week 1, (c,d) week 3, and (e,f) week 5 forecasts. The set of the maps is average of the three sets of forecasts using

three different MJO/BSISO indices. Areas of stippling indicate that the HSS is significant at the 5% level.

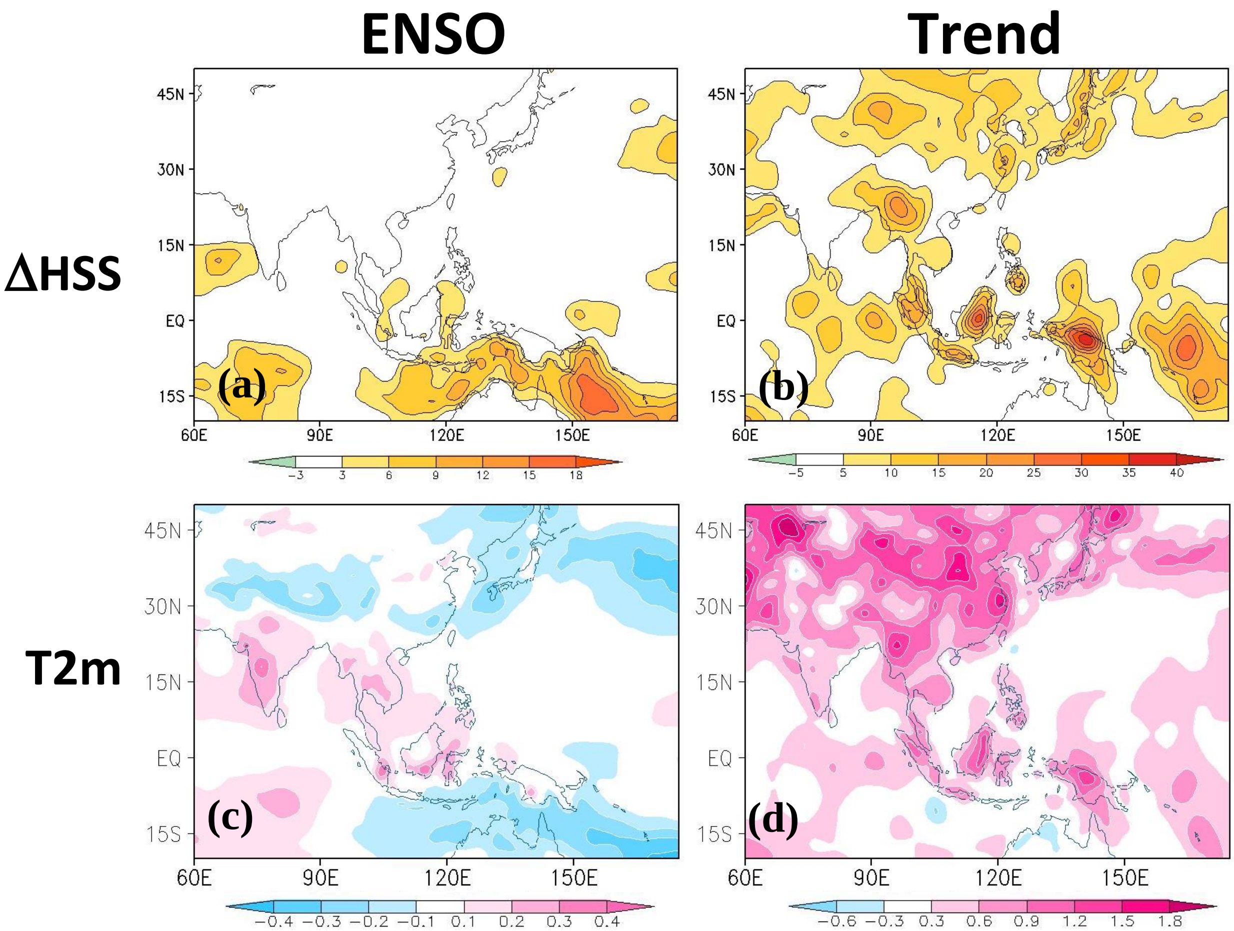

Figure 2. ENSO and linear trend contributions to T2m forecast skill. Week 1 HSS differences between the full prediction model and models that exclude (a) ENSO and (b) linear trend. Regression coefficients for T2m anomalies regressed on (c) the Niño 3.4 index (°C $°C^{-1}$) and (d) time (linear trend) (°C $[30yr]^{-1}$).

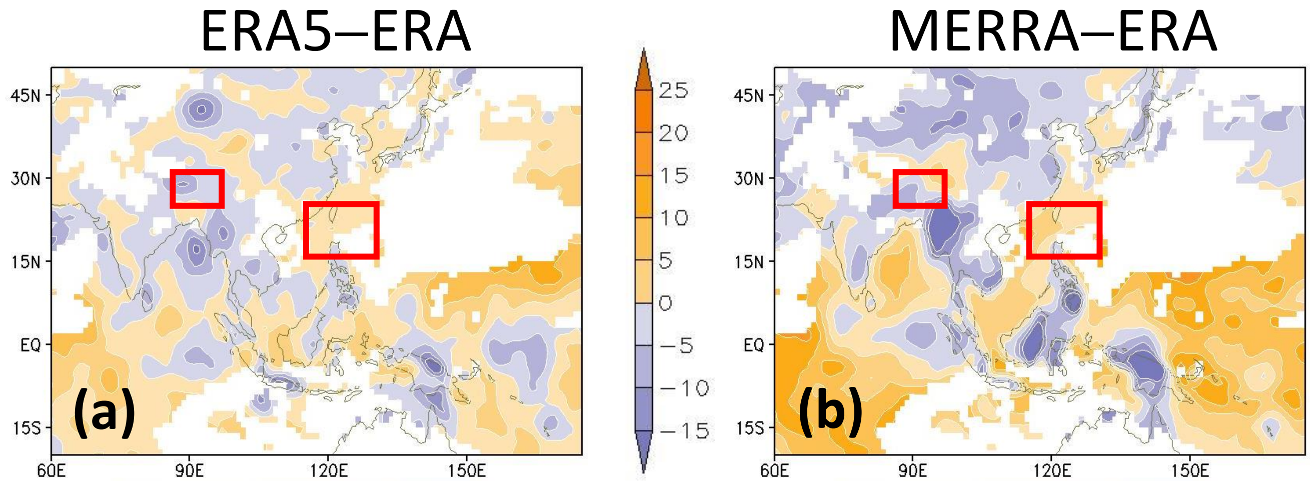

Figure 3. Sensitivity of T2m forecast skill to dataset. ΔHSS maps of the full forecasts using (a) ERA5 and (b) MERRA relative to that of ERA-Interim for week one. The red boxes mark the Tibet and Taiwan-Philippine regions (see section 3.2).

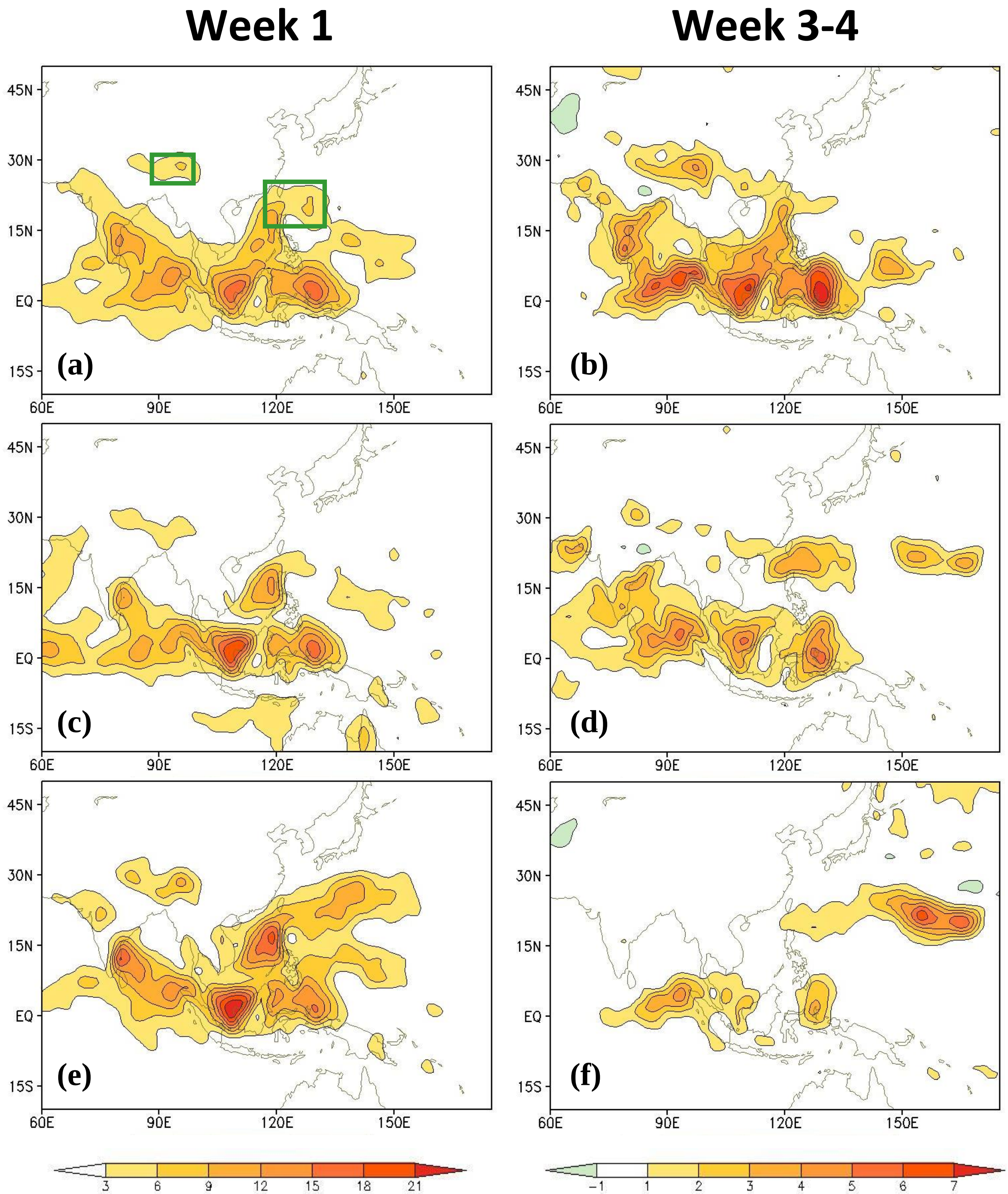

Figure 4. Sensitivity of T2m forecast skill to MJO/BSISO index. ΔHSS for forecasts with and without the (top) Bimodal, (middle) WH MJO, and (bottom) JYL MJO/BSISO index predictors. Left panels are for week 1 forecasts and right panels are for ΔHSS averaged

for weeks 3 and 4 forecasts. The green boxes in (a) mark the Tibet and Taiwan-Philippine regions (see section 3.2).

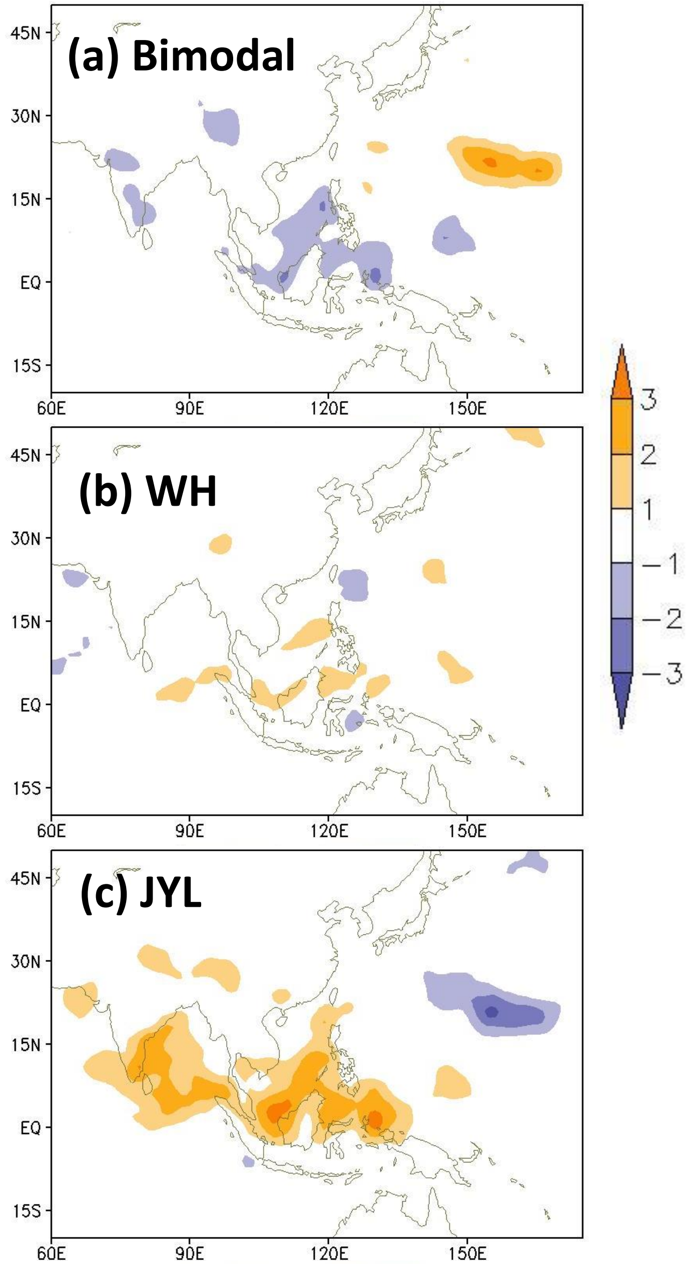

Figure 5. ΔHSS for week 1 T2m forecasts between three-model ensemble mean and (a) Bimodal, (b) WH, and (c) JYL indices.

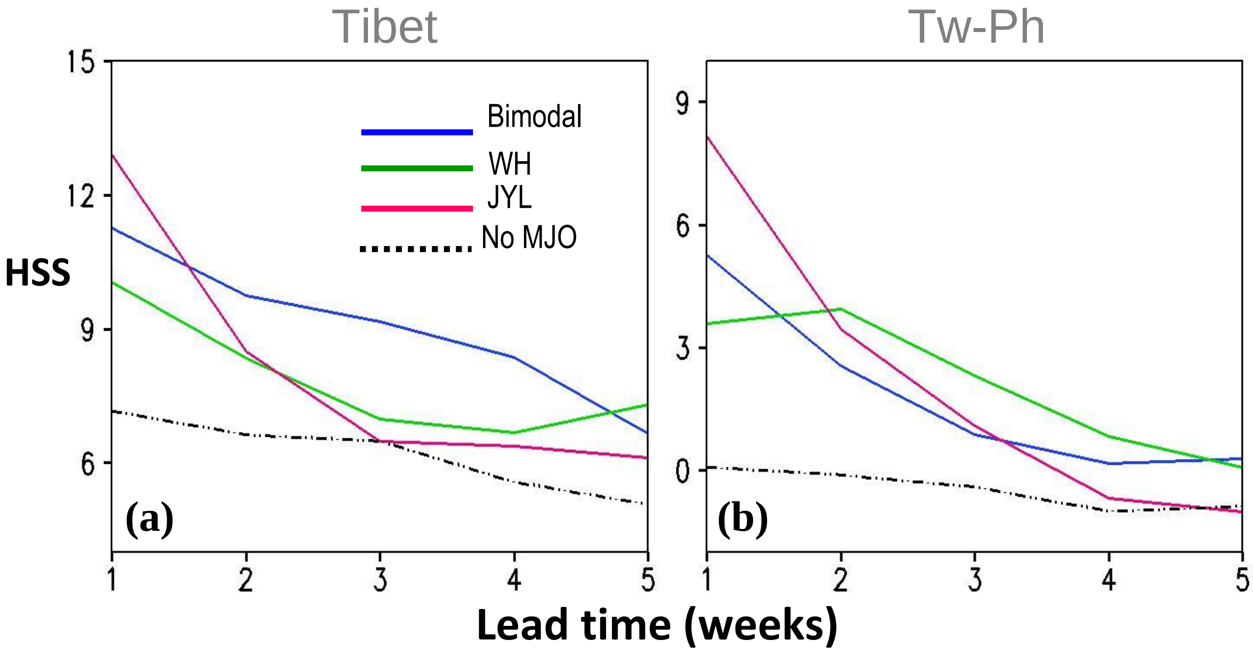

Figure 6. Average T2m forecast skill in the Taiwan-Philippines (Tw-Ph) and Tibet regions with different MJO/BSISO predictors. Mean HSS (y-axis) averaged over the (a) Tw-Ph and (b) Tibet regions as function of lead time (x-axis, in weeks), with the Bimodal (blue), WH MJO (green), and JYL (magenta) indices used as predictors. The dashed black line indicates the mean skill for forecasts with the MJO/BSISO index excluded as a predictor. The two regions are defined by green boxes in Fig. 3.

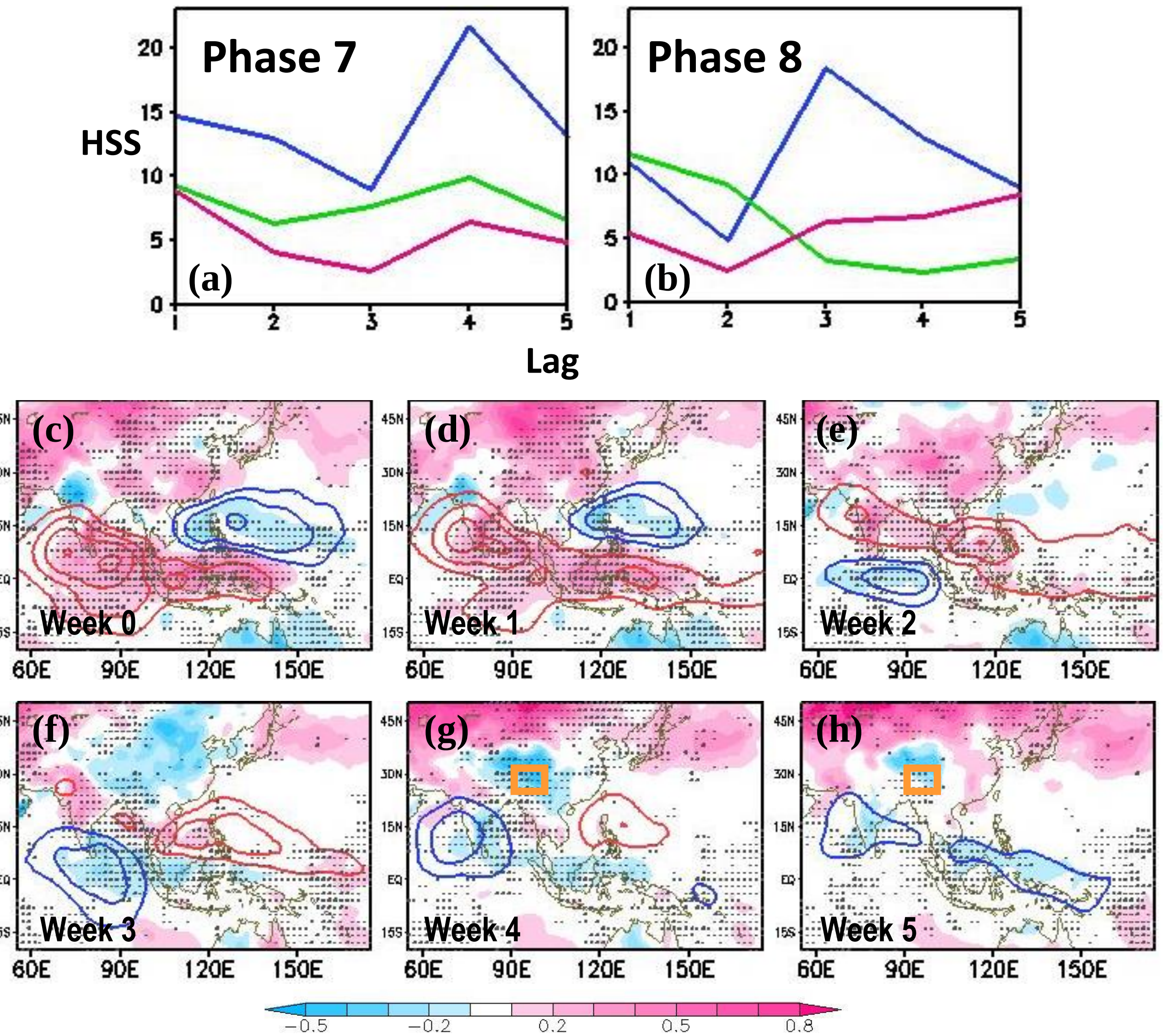

Figure 7. Windows of subseasonal T2m forecast opportunity in Tibet region following MJO/BSISO phases 7 and 8. Mean May-October HSS over the Tibet region (see orange box in panels g and h) for weeks 1-5 (x-axis) following MJO/BSISO phase (a) 7 and (b) 8 for forecasts that use the Bimodal index predictor (blue), WH MJO index predictor (green), and JYL BSISO index predictor (magenta). (c-h) Week 0 through week 5 composite anomalies of T2m (color shading, °C) and OLR (color contours with a minimum magnitude of 5 for both positive (red) and negative (blue) values; interval = 5 Wm^{-2}), following Bimodal index phase 7. Areas of stippling indicate that the HSS is significant at the 5% level.

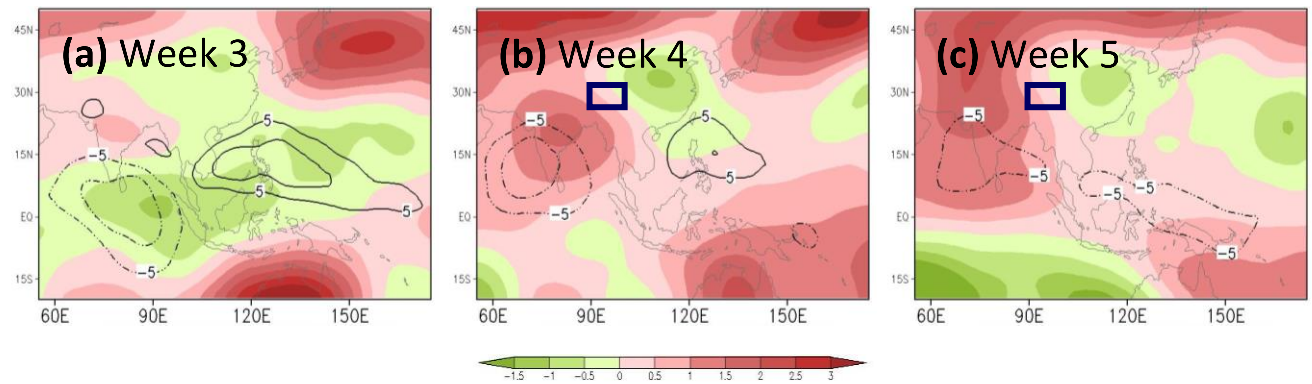

Figure 8. Composite anomalies of 300 hPa streamfunction (color, $\times 10^{-6}$ s^{-1}) and OLR (contour, interval = 5 Wm^{-2}) following Bimodal index phase 7 for (a) week 3, (b) week 4, and (c) week 5. The blue box in (b) & (c) denote the Tibet region.

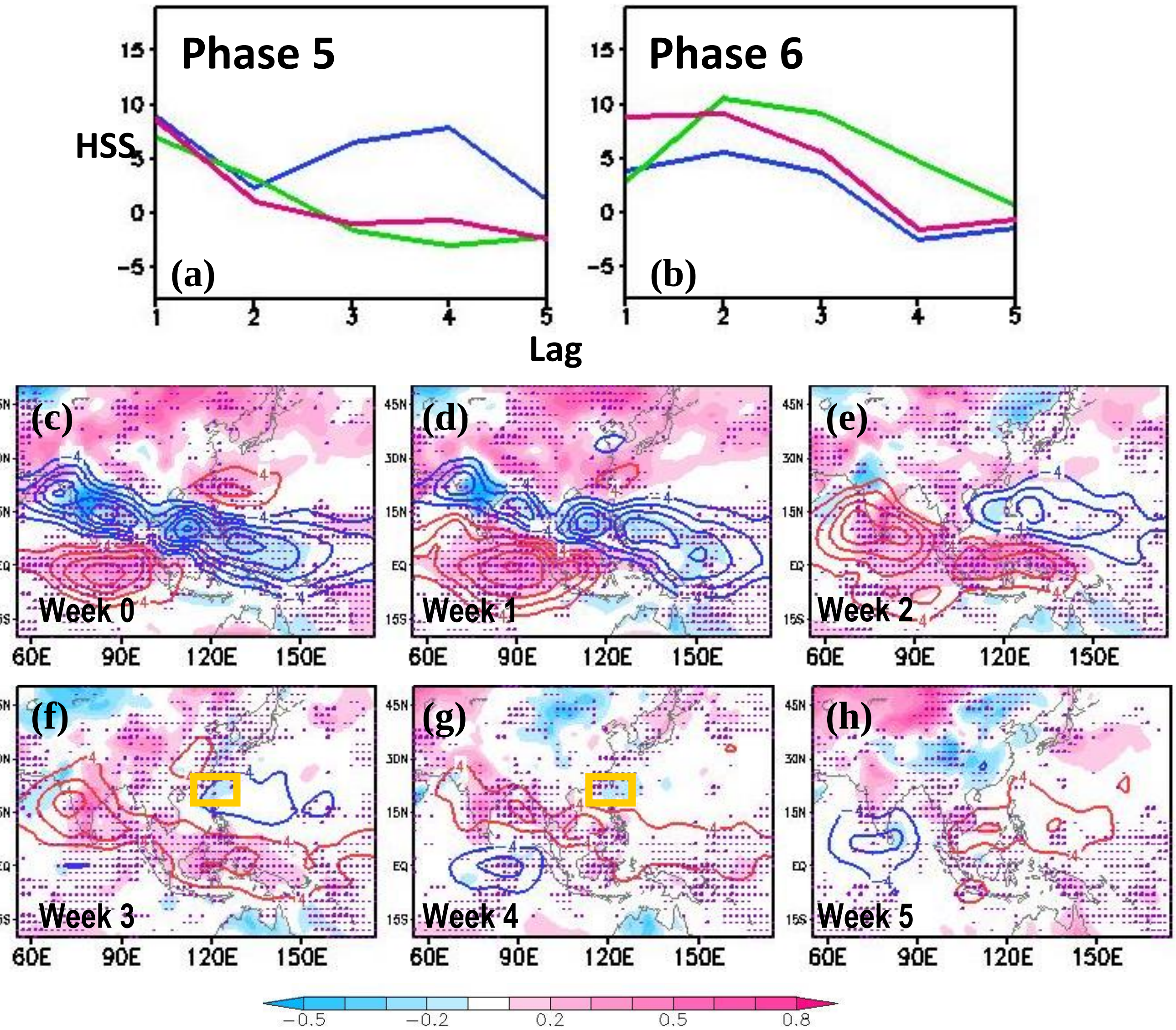

Figure 9. Windows of subseasonal T2m forecast opportunity in Taiwan-Philippine region following MJO/BSISO phases 5 and 6. (a,b) As in Fig. 7 but for the Taiwan-Philippine region (orange box in panels f and g) and following MJO/BSISO phase 5 and 6, respectively. (c-h) Week 0 through week 5 composite anomalies of T2m (color shading, °C) and OLR (contours; interval = 4 Wm^{-2}) following Bimodal index phase 5. Areas of stippling indicate that the HSS is significant at the 5% level.

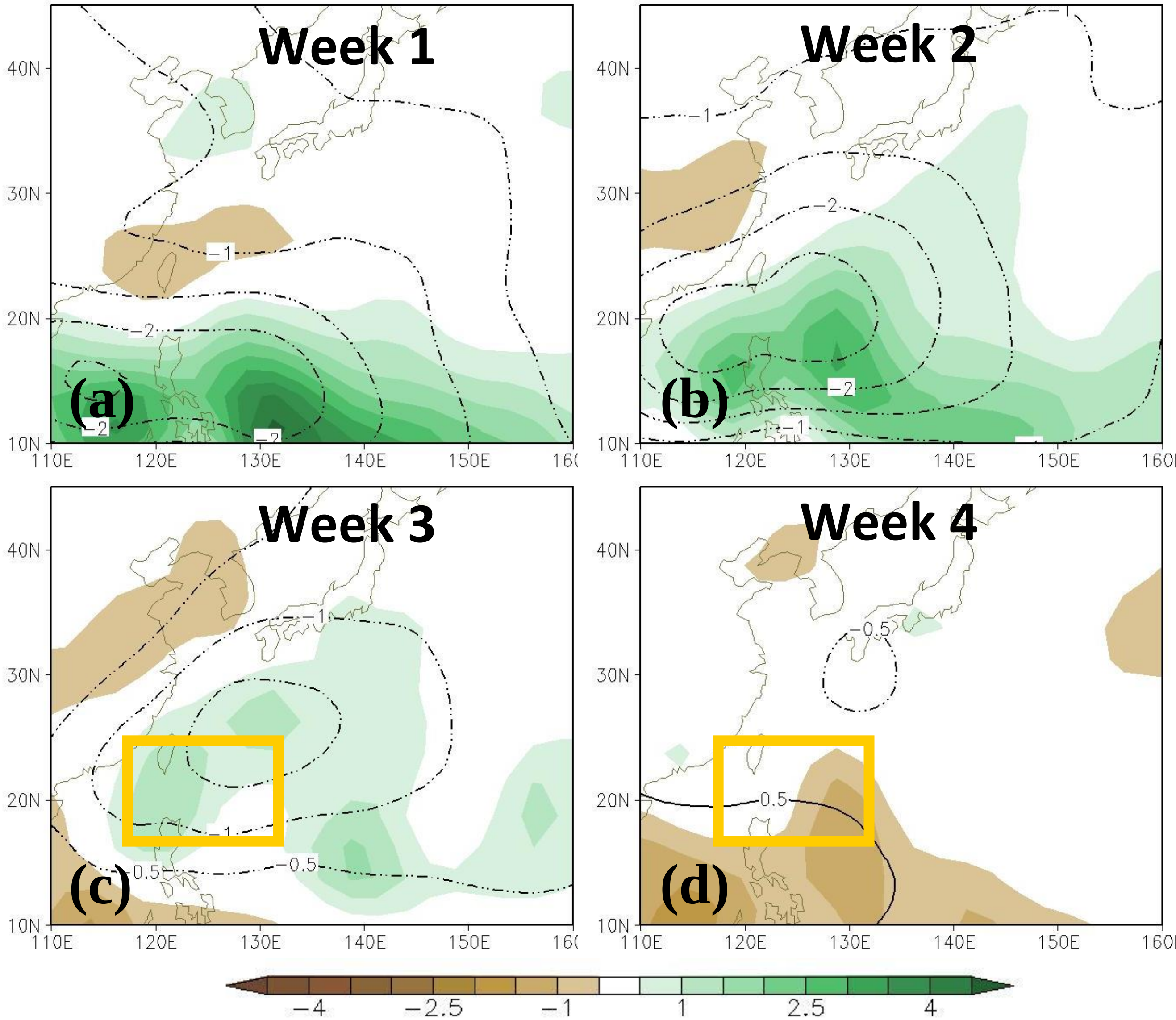

Figure 10. Composites anomalies of precipitation (color shading; mm day^{-1}) and 850 hPa streamfunction (contours, interval = 0.5 $\times 10^{-6}$ s^{-1}) in Taiwan-Philippine region following Bimodal index phase 5 (a-d) week 1 through week 4.

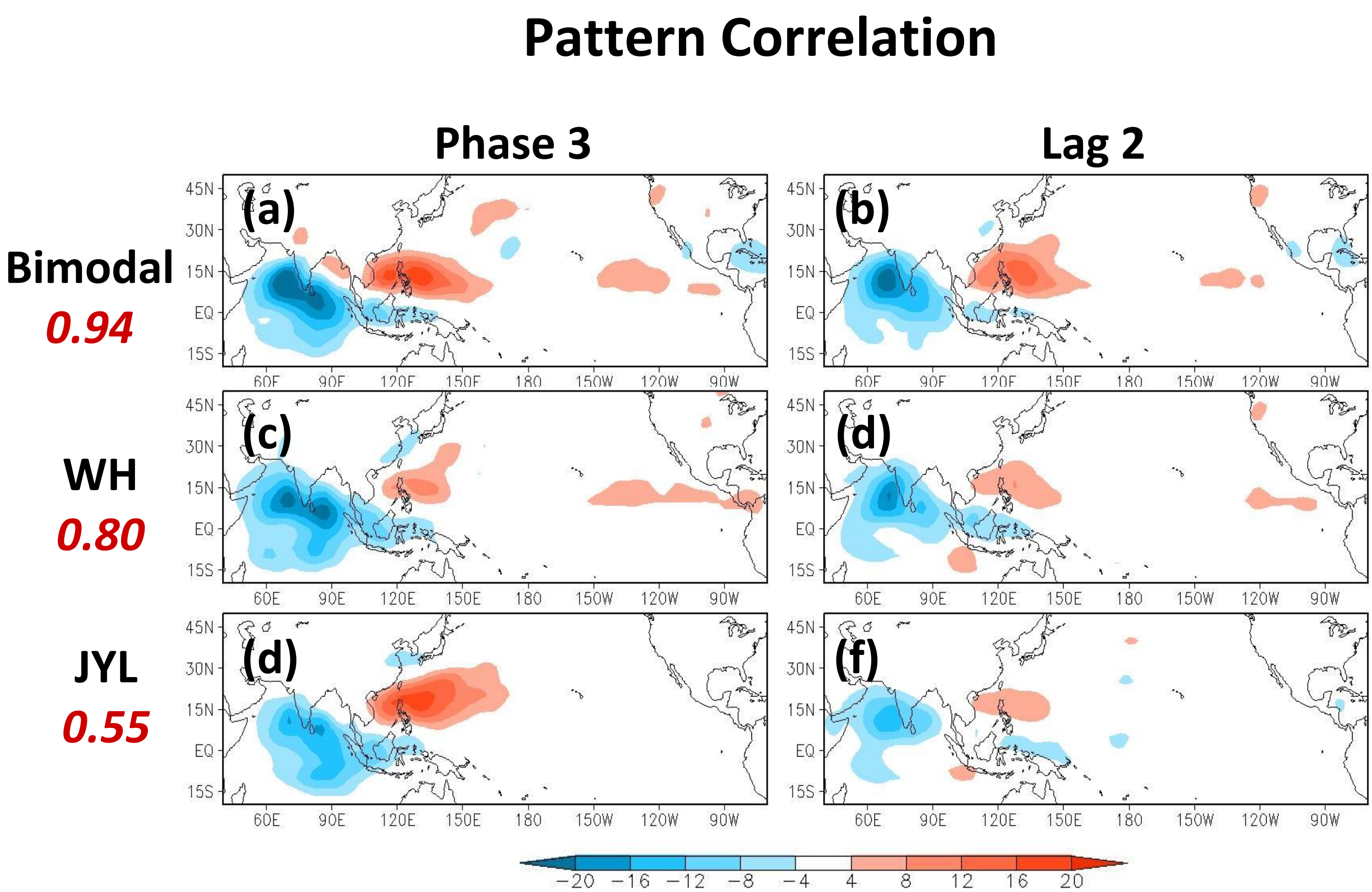

Figure 11. OLR composite for (left) MJO/BSISO phase 3 and (right) lag 2 (averaged 8-14 days after the onset of phase 1) with respect to phase 1 for each index: (top) Bimodal, (middle) WH, and (bottom) JYL index. The pattern correlation coefficients are noted underneath the respective indices on the left. Lags are in weeks.

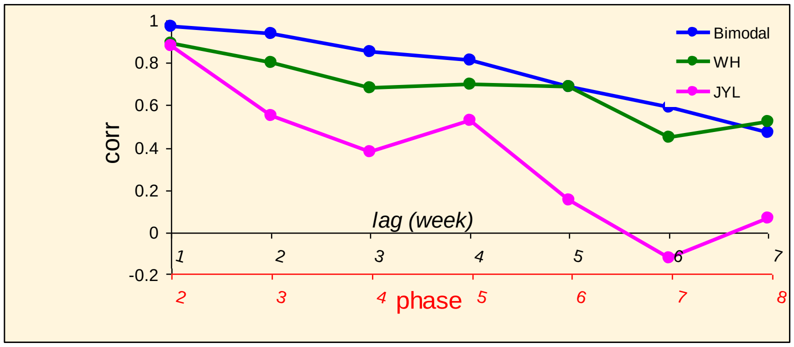

Figure 12. Pattern correlation coefficient between the MJO/BSISO OLR composite sorted by phase (indicated by red x-axis) and lagged OLR composite with respect to phase 1 onset (with lag indicated by the black x-axis) for each index: Bimodal (blue), WH (green) and JYL (magenta) index. Lags are in weeks.